Magnetic Properties of $RE_3Pd_6Sb_5$ (RE = Pr, Nd, Gd) and a Group-Subgroup Scheme for $Ce_3Pd_6Sb_5$ and $Yb_5Cu_{11}Sn_8$

Inga Schellenberg, Rolf-Dieter Hoffmann, Stefan Seidel, Christian Schwickert, and Rainer Pöttgen

Institut für Anorganische und Analytische Chemie, Universität Münster, Corrensstraße 30, 48149 Münster, Germany

Reprint requests to R. Pöttgen. E-mail: pottgen@uni-muenster.de

Z. Naturforsch. **2011**, *66b,* 985 – 992; received September 26, 2011

The $Ce_3Pd_6Sb_5$-type antimonides $RE_3Pd_6Sb_5$ (RE = Pr, Nd, Sm, Gd, Tb) were synthesized by arc-melting and subsequent annealing in sealed silica ampoules in a high-frequency furnace. The new compounds $Sm_3Pd_6Sb_5$ (a = 1337.0(5), b = 441.5(1), c = 988.6(3) pm) and $Tb_3Pd_6Sb_5$ (a = 1328.8(4), b = 439.9(2), c = 976.6(5) pm) were characterized by powder X-ray diffraction data. The $RE_3Pd_6Sb_5$ antimonides adopt an ordered defect structure that derives from the $CaBe_2Ge_2$ type. Their crystal chemistry is compared to the structures of $Ce_8Rh_{17}Sb_{14}$ and $Yb_5Cu_{11}Sn_8$ on the basis of group-subgroup schemes. Temperature-dependent magnetic susceptibility data of the samples with RE = Pr, Nd and Gd show Curie-Weiss paramagnetism of the trivalent rare earths. Low-field susceptibility measurements reveal magnetic ordering at low temperatures.

Key words: Antimony, Intermetallics, Magnetic Properties, Group-Subgroup Schemes

Introduction

The $ThCr_2Si_2$ ($I4/mmm$) [1] and $CaBe_2Ge_2$ ($P4/nmm$) [2] type structures are ordered variants of the well known $BaAl_4$ type [3]. Of the more than 1000 representatives of this structural family, several examples show extended homogeneity ranges and, furthermore, diverse RT_2X_2 compounds (R = alkali, alkaline earth, rare earth, or actinoid metal; T = transition metal; X = element of the 3rd, 4th, or 5th main group) can feature significant defects, either $RT_{2-x}X_2$ or RT_2X_{2-y} [4, 5]. Such defects may be only statistical and account for adjustment of the valence electron concentration, but in many cases well ordered superstructures with defined compositions are formed. Prominent examples are the structures of $Eu_2Au_2Sn_5 \equiv EuAuSn_{2.5}$ [6], $Ce_3Pd_6Sb_5 \equiv CePd_2Sb_{1.66}$ [7], $Yb_3Au_{5.5}Ga_{5.5} \equiv YbAu_{1.83}Ga_{1.83}$ [8], or $Dy_3Co_6Sn_5 \equiv DyCo_2Sn_{1.66}$ [9]. A recent example is the antimonide $Ce_8Rh_{17}Sb_{14}$ [10] which shows an ordering of antimony vacancies.

In continuation of our systematic studies of $BaAl_4$-related superstructures [6, 10, 11] we have extended the investigations on antimonides with the $Ce_3Pd_6Sb_5$-type structure [7]. Besides the prototype itself, the structures of $RE_3Pd_6Sb_5$ with RE = Pr, Nd, Gd [12] have been reported. Magnetic data are only available for the cerium compound. $Ce_3Pd_6Sb_5$ is a Curie-Weiss paramagnet which orders antiferromagnetically at T_N = 6 K [7]. Herein we report on the magnetic properties of the remaining compounds and the synthesis of the new antimonides $Sm_3Pd_6Sb_5$ and $Tb_3Pd_6Sb_5$. Furthermore we developed a group-subgroup scheme for the structures of $Ce_3Pd_6Sb_5$ and $Yb_5Cu_{11}Sn_8$ [13] which show an ordering pattern similar to $Ce_8Rh_{17}Sb_{14}$ [10].

Experimental Section

Synthesis

Starting materials for the synthesis of the $RE_3Pd_6Sb_5$ (RE = Pr, Nd, Sm, Gd, Tb) samples were ingots of the rare earth elements (Johnson Matthey or smart elements), palladium powder (Degussa-Hüls) and antimony shots (Johnson Matthey), all with stated purities better than 99.9 %. In a first step, small pieces of the rare earth ingots were arc-melted [14] under argon (*ca.* 700 mbar) to buttons. The argon was purified before with molecular sieves, silica gel, and titanium sponge (900 K). The pre-melting procedure strongly reduces shattering during the subsequent, strongly exothermic reactions with palladium and antimony. The elements were then weighed in the atomic ratio 3 : 6 : 5 and arc-melted three times on each side to ensure homogeneity. The total weight loss after the melting procedure was less than 0.5 %. Subsequently the arc-melted buttons were sealed in evacuated silica tubes and annealed for 30 to 40 min in an in-

Table 1. Lattice parameters of the orthorhombic antimonides $RE_3Pd_6Sb_5$.

Compound	a (pm)	b (pm)	c (pm)	V (nm^3)	Reference
$Ce_3Pd_6Sb_5$	1348.1(2)	445.9(1)	1005.0(1)	0.6041	[7]
$Pr_3Pd_6Sb_5$	1344.7(5)	445.9(1)	999.6(3)	0.5994	this work
$Pr_3Pd_6Sb_5$	1344.2(3)	444.2(2)	999.4(2)	0.5967	[12]
$Nd_3Pd_6Sb_5$	1341.7(3)	443.5(1)	996.8(2)	0.5931	this work
$Nd_3Pd_6Sb_5$	1341.2(3)	443.1(1)	996.2(2)	0.5920	[12]
$Sm_3Pd_6Sb_5$	1337.0(5)	441.5(1)	988.6(3)	0.5836	this work
$Gd_3Pd_6Sb_5$	1330.7(4)	440.0(1)	986.7(3)	0.5777	this work
$Gd_3Pd_6Sb_5$	1329.3(2)	439.7(1)	988.1(2)	0.5775	[12]
$Tb_3Pd_6Sb_5$	1328.8(4)	439.9(2)	976.6(5)	0.5709	this work

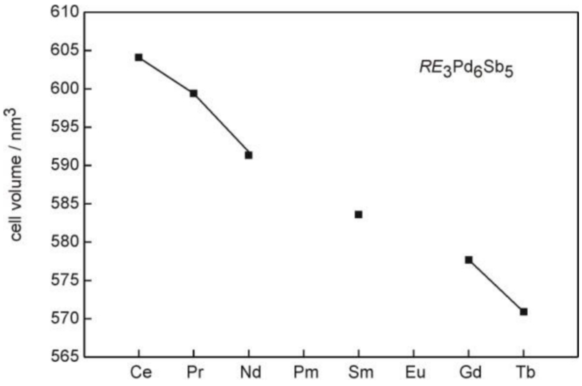

Fig. 1. Course of the cell volume of the orthorhombic antimonides $RE_3Pd_6Sb_5$.

duction furnace (Hüttinger Elektronik, Freiburg, Typ TIG 1.5/300 [15]) slightly below the melting point. The resulting polycrystalline samples are silvery with metallic luster. They are stable in air over several weeks.

X-Ray diffraction

The polycrystalline $RE_3Pd_6Sb_5$ samples were characterized by Guinier powder patterns (Cu$K_{\alpha1}$ radiation, α-quartz: a = 491.30, c = 540.46 pm as internal standard). The Guinier camera was equipped with an imaging plate unit (Fuji film, BAS-READER 1800). The orthorhombic lattice parameters (Table 1) were obtained from least-squares fits. Proper indexing was ensured by intensity calculations [16].

Physical property measurements

The magnetic measurements were carried out on a Quantum Design Physical Property Measurement System (PPMS) using the VSM option. For VSM measurements, the samples (7.353 mg for $Pr_3Pd_6Sb_5$, 14.366 mg for $Nd_3Pd_6Sb_5$, 12.735 mg for $Gd_3Pd_6Sb_5$) were packed in kapton foil and attached to the sample holder rod for measuring the magnetic properties in the temperature range 2.5 – 305 K with magnetic flux densities up to 80 kOe.

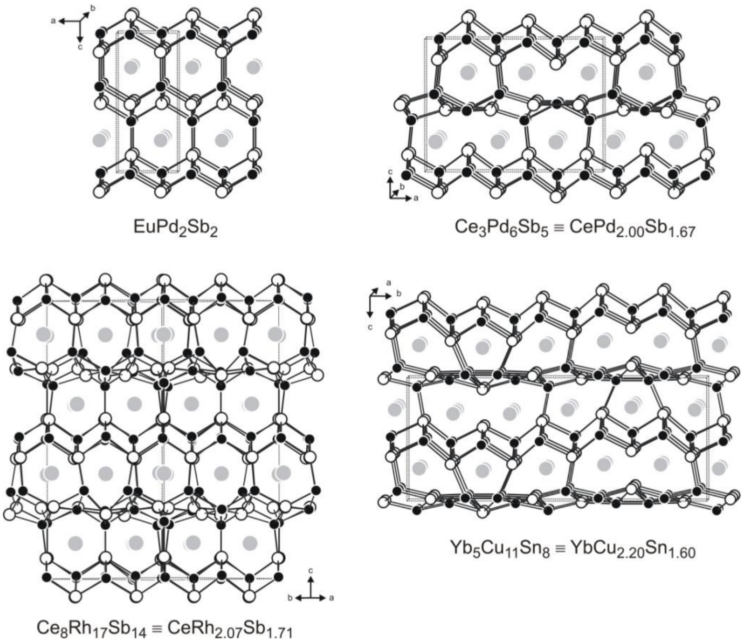

$EuPd_2Sb_2$

$Ce_3Pd_6Sb_5 \equiv CePd_{2.00}Sb_{1.67}$

$Ce_8Rh_{17}Sb_{14} \equiv CeRh_{2.07}Sb_{1.71}$

$Yb_5Cu_{11}Sn_8 \equiv YbCu_{2.20}Sn_{1.60}$

Fig. 2. The crystal structures of $EuPd_2Sb_2$, $Ce_3Pd_6Sb_5$, $Ce_8Rh_{17}Sb_{14}$, and $Yb_5Cu_{11}Sn_8$. Rare earth, transition metal, and antimony (tin) atoms are drawn as medium grey, black filled, and open circles, respectively. The three-dimensional [Pd_2Sb_2], [Pd_6Sb_5], [$Rh_{17}Sb_{14}$], and [$Cu_{11}Sn_8$] networks are emphasized.

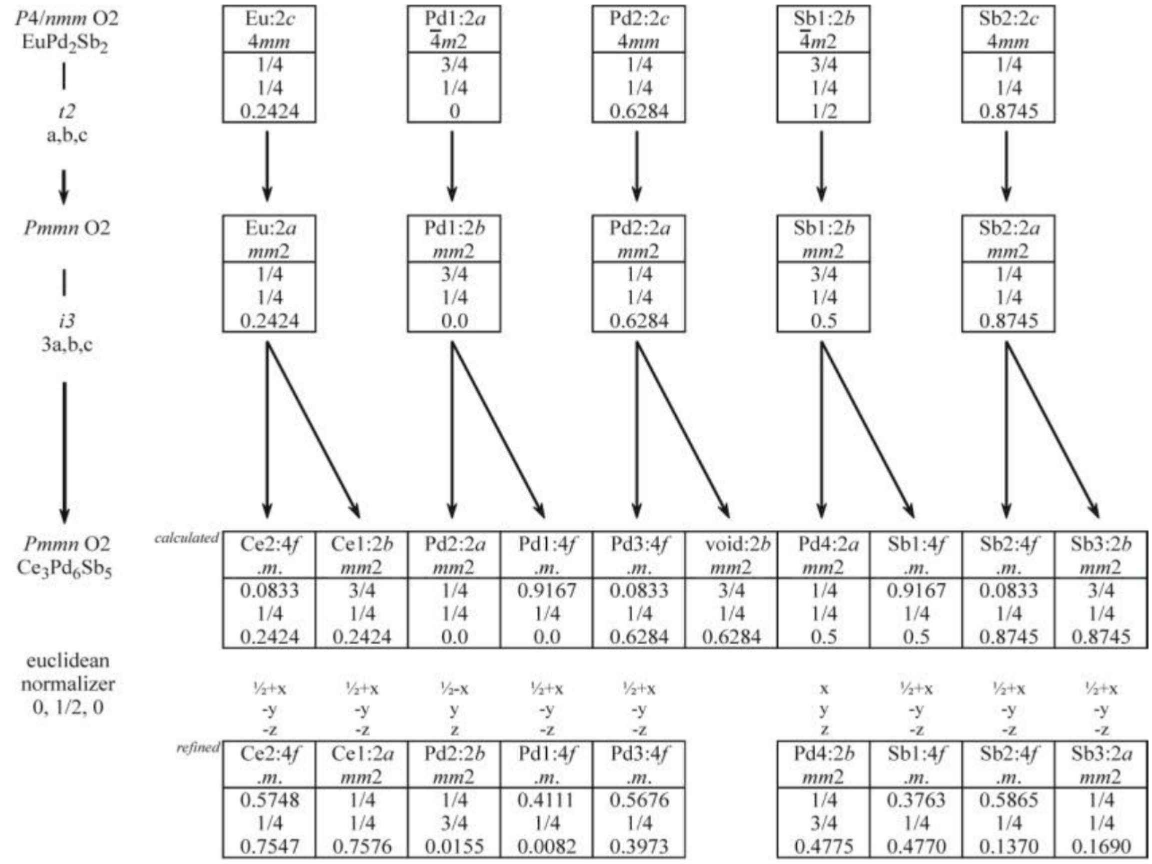

Fig. 3. Group-subgroup scheme in the Bärnighausen formalism [19 – 22] for the structures of $EuPd_2Sb_2$ [17] and $Ce_3Pd_6Sb_5$ [7]. The indices for the *isomorphic* (i) symmetry reductions, the unit cell transformations, and the evolution of the atomic parameters are given.

Discussion

Crystal chemistry

The $RE_3Pd_6Sb_5$ antimonides exist with Ce, Pr, Nd, Sm, Gd, and Tb as the rare earth element. $Sm_3Pd_6Sb_5$ and $Tb_3Pd_6Sb_5$ are new compounds. The cell volumes (Table 1) decrease from the cerium to the terbium compound (Fig. 1) as expected from the lanthanide contraction. $Ce_3Pd_6Sb_5$ smoothly fits into that curve, indicating trivalent cerium, in agreement with the magnetic data [7].

The subcell structure of $Ce_3Pd_6Sb_5$ resembles that of $CaBe_2Ge_2$-type $EuPd_2Sb_2$ [17]. In both structures (Fig. 2) the palladium and antimony atoms build up three-dimensional [Pd_6Sb_5] and [Pd_2Sb_2] networks which leave larger cavities for the rare earth elements. The Pd–Sb distances in these networks range from 263 to 281 pm in $Ce_3Pd_6Sb_5$ and from 267 to 268 pm in $EuPd_2Sb_2$ [17]. These Pd–Sb distances are close to the sum of the covalent radii [18] of 269 pm, indicating substantial Pd–Sb bonding in both antimonides. In $EuPd_2Sb_2$ we observe layers of edge-sharing $PdSb_{4/4}$ tetrahedra at $z = 0$ and the inverse arrangement, *i. e.* layers of edge-sharing $SbPd_{4/4}$ tetrahedra, at $z = 1/2$ (Fig. 2). The first type of layer is also observed in the structure of $Ce_3Pd_6Sb_5$. In contrast, the second layer in $Ce_3Pd_6Sb_5$ shows defects and strong distortions. This kind of atomic arrangement reminds of the recently determined structure of $Ce_8Rh_{17}Sb_{14}$ [10]. Although this structure looks quite complex at first sight (Fig. 2), the distortions and defect formations strictly follow a group-subgroup scheme, leading to a concise and compact description of the structure. Another structurally closely related compound is the stannide $Yb_5Cu_{11}Sn_8$ [13]. In the following chapter we work out the group-subgroup schemes

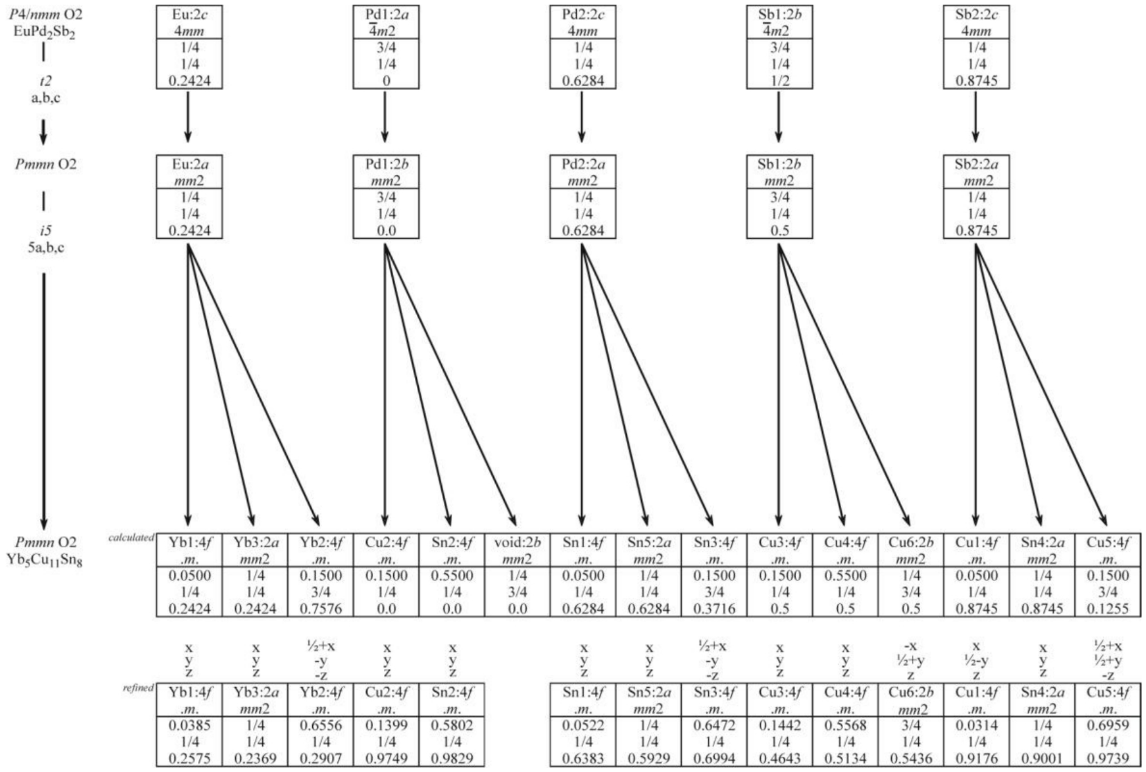

Fig. 4. Group-subgroup scheme in the Bärnighausen formalism [19 – 22] for the structures of $EuPd_2Sb_2$ [17] and $Yb_5Cu_{11}Sn_8$ [13]. The indices for the *isomorphic* (i) symmetry reductions, the unit cell transformations, and the evolution of the atomic parameters are given. The refined atomic parameters of $Yb_5Cu_{11}Sn_8$ are given in the *bac* setting as compared to the published data.

for $Ce_3Pd_6Sb_5$ and $Yb_5Cu_{11}Sn_8$ in the Bärnighausen formalism [19 – 22].

Group-subgroup scheme for $Ce_3Pd_6Sb_5$ and $Yb_5Cu_{11}Sn_8$

Comparing the highly symmetric $EuPd_2Sb_2$ structure [17] with those of $Ce_3Pd_6Sb_5$ and $Yb_5Cu_{11}Sn_8$ it becomes evident that the cerium compound has a tripled and the ytterbium compound a quintupled unit cell. Both compounds crystallize with space group type *Pmmn*. Starting from $EuPd_2Sb_2$ (*P*4/*nmm*) the space group symmetry is first reduced to *Pmmn via* a *translationengleiche* reduction of index 2 (t2). The next steps are isomorphic transitions, i3 for $Ce_3Pd_6Sb_5$ and i5 for $Yb_5Cu_{11}Sn_8$ (Figs. 3 and 4). Both Bärnighausen trees readily reveal the formation of one ordered defect in each of the structure types.

In order to understand the ordering of the palladium (copper) and antimony (tin) atoms and the defects within the strongly distorted layers we have first calculated the ideal positions, starting from the setting of $EuPd_2Sb_2$ [17]. For both superstructure variants the coloring within the defect layers is different as compared to the stoichiometric layers. In the latter one observes an almost regular arrangement of edge-sharing $PdSb_{4/4}$ and $CuSn_{4/4}$ tetrahedra (Fig. 2). Around the defects (Figs. 5 and 6) there is an accumulation of palladium, respectively copper atoms. In going from the ideal, calculated model to the refined structure, the coordination around the ordered defects drastically changes with a strong shift of the antimony (in $Ce_3Pd_6Sb_5$) and copper (in $Yb_5Cu_{11}Sn_8$) atoms towards the defect position. These structural distortions lead to a significant decrease of the metal–metal distances in both layers. The Cu–Cu (245 – 260 pm) and Pd–Pd (276 pm) distances are close to those in *fcc* copper (256 pm) and *fcc* palladium (275 pm) [23], and one can conclude that metal-metal bonding might be the driving force for superstructure formation. The strong distortions have drastic effects on the course of the lat-

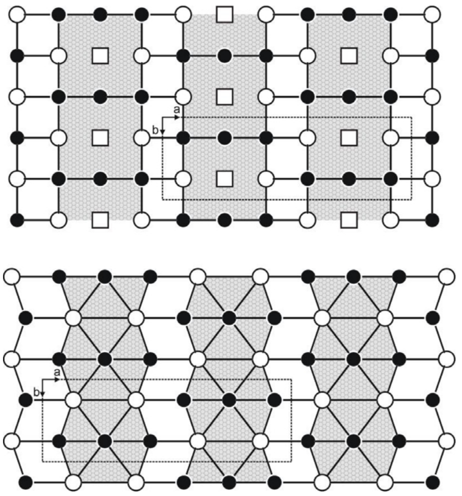

Fig. 5. Cutout of the defect layer of the $Ce_3Pd_6Sb_5$ structure (•: Pd, ○: Sb). The upper part of the drawing shows the ideal structure (see the group-subgroup scheme in Fig. 3) with ordered vacancies (open squares). The refined structure is presented below. The characteristic building units around the defects are shaded.

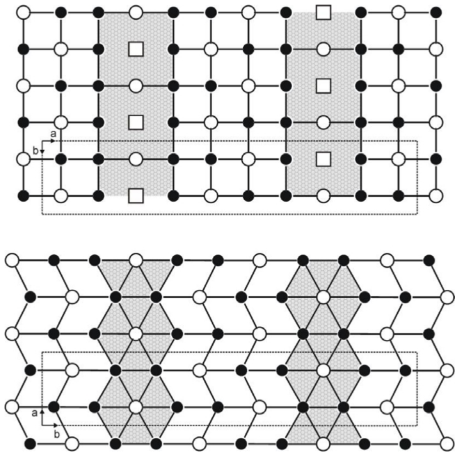

Fig. 6. Cutout of the defect layer of the $Yb_5Cu_{11}Sn_8$ structure (•: Cu, ○: Sn). The upper part of the drawing shows the ideal structure (see the group-subgroup scheme in Fig. 4) with ordered vacancies (open squares). The refined structure is presented below. The characteristic building units around the defects are shaded.

tice parameters: the subcell parameters of $1/3a = 449.4$ and $b = 445.9$ pm for $Ce_3Pd_6Sb_5$ and $1/5b = 453.1$ and $a = 442.7$ pm for $Yb_5Cu_{11}Sn_8$ deviate significantly from tetragonality.

From a group-theoretical point of view also an ordered superstructure with an isomorphic transition of index seven (i7) is imaginable. However, it is questionable if such a long translation period is realized over larger domains (several hundred unit cells) so that superstructure reflections would be detectable. In the large family of KHg_2 superstructures [24], so far only i5 variants have been observed [25, 26].

Table 2. Magnetic data of the antimonides $RE_3Pd_6Sb_5$ (RE = Pr, Nd, Gd): μ_{eff}, experimental effective moment; μ_{calc}, theoretical magnetic moment; θ_P, paramagnetic Curie temperature; T_O, magnetic ordering temperature.

Compound	μ_{eff} (μ_B/RE)	μ_{calc} (μ_B/RE^{3+})	θ_P (K)	T_O (K)
$Pr_3Pd_6Sb_5$	3.53(1)	3.58	−3.8(5)	4.3(3)
$Nd_3Pd_6Sb_5$	3.64(1)	3.62	−6.2(5)	11.7(1)
$Gd_3Pd_6Sb_5$	8.01(1)	7.94	−24.7(5)	8.4(1)

Finally it is interesting to note that a stannide of composition $Yb_3Cu_6Sn_5$ [13] also exists, however, this compound crystallizes with the body-centered $Dy_3Co_6Sn_5$-type structure [9], space group *Immm*, and can be considered a ternary ordered version of La_3Al_{11} (defect variants of $BaAl_4$ resp. $ThCr_2Si_2$). Thus, two stannides, $YbCu_{2.00}Sn_{1.66}$ and $YbCu_{2.20}Sn_{1.60}$, with close composition but different copper-tin ordering exist. Minor differences in composition lead to a distinct reorganization of the polyanionic network.

Magnetic properties of $RE_3Pd_6Sb_5$ (RE = Pr, Nd, Gd)

The temperature-dependent susceptibility and inverse susceptibility (χ(T) and χ^{-1}(T) data) measured at an externally applied field of 10 kOe of a) $Pr_3Pd_6Sb_5$, b) $Nd_3Pd_6Sb_5$ and c) $Gd_3Pd_6Sb_5$ are depicted in Fig. 7. In all three cases it was possible to fit the susceptibility data in the temperature range from 20 to 300 K with the Curie-Weiss law. We were able to determine the effective magnetic moments as well as the Weiss constants of the studied compounds from these fits. The magnetic properties are listed in Table 2. The effective magnetic moments are in agreement with the theoretical values according to $g_J(J(J+1))^{1/2}$. In addition, the negative values of the Weiss constants are indicative of antiferromagnetic interactions in the paramagnetic regions.

In addition to the standard zero-field-cooled measurements at 10 kOe, supplementary measurements were performed in *zero-field-cooled/field-cooled* mode at an externally applied field of 100 Oe. The resulting temperature-dependent susceptibilities are depicted in Fig. 8. Noticeably the ZFC and FC data diverge from one another for all three compounds. The respective temperatures for the divergence can be deduced from Figs. 8a–c, *i. e.* 3.1 K for $Pr_3Pd_6Sb_5$ (*cf.* inset

a) $Pr_3Pd_6Sb_5$

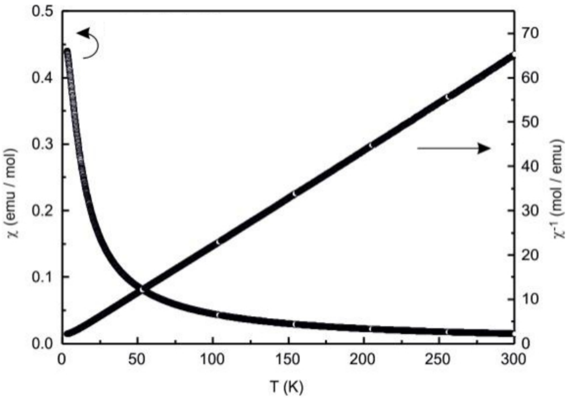

b) $Nd_3Pd_6Sb_5$

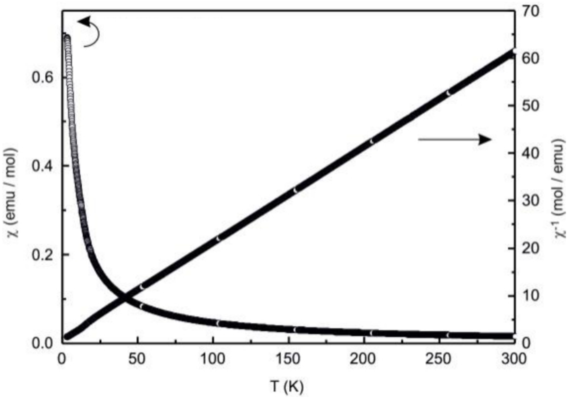

c) $Gd_3Pd_6Sb_5$

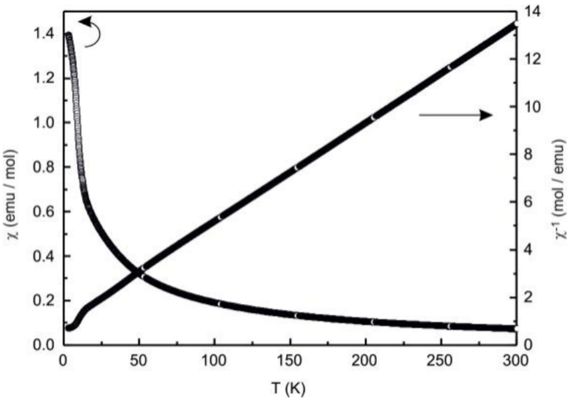

Fig. 7. Temperature dependence of the magnetic susceptibility (χ and χ^{-1} data) of a) $Pr_3Pd_6Sb_5$, b) $Nd_3Pd_6Sb_5$ and c) $Gd_3Pd_6Sb_5$ measured at 10 kOe.

a) $Pr_3Pd_6Sb_5$

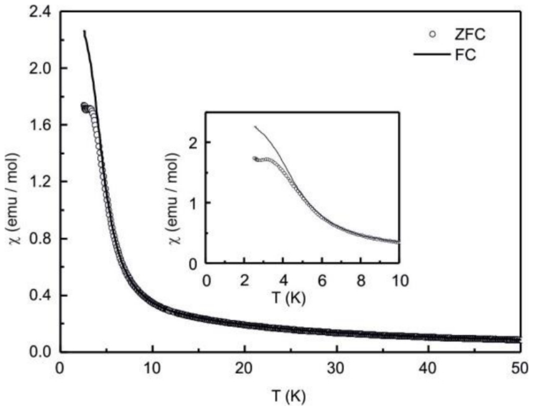

b) $Nd_3Pd_6Sb_5$

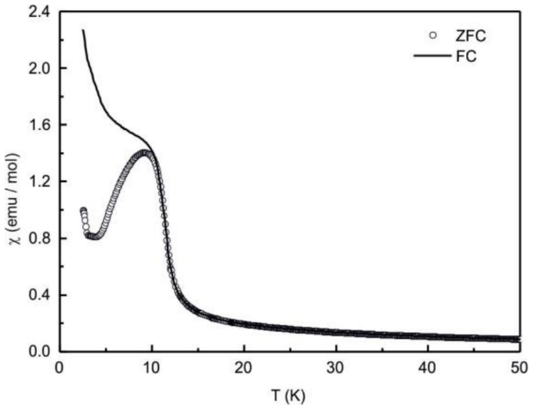

c) $Gd_3Pd_6Sb_5$

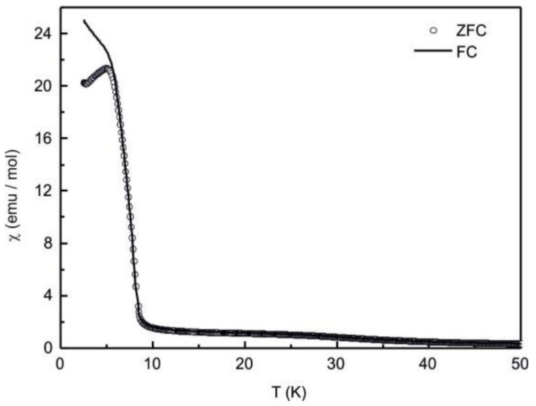

Fig. 8. Temperature dependence of the magnetic susceptibility (χ data) of a) $Pr_3Pd_6Sb_5$, b) $Nd_3Pd_6Sb_5$ und c) $Gd_3Pd_6Sb_5$ measured at 100 Oe in *zero-field-cooled/field-cooled* mode.

Fig. 8a), 9.1 K for $Nd_3Pd_6Sb_5$ (Fig. 8b), and 4.9 K for $Gd_3Pd_6Sb_5$ (Fig. 8c). These divergencies are indicative of spin glass anomalies in the three antimonides. Also based on the magnetization isotherms (*vide infra*), no clear antiferromagnetic or ferromagnetic ground state can be attributed to $RE_3Pd_6Sb_5$ (RE = Pr, Nd, Gd). The onset of magnetic ordering is detected at 4.3(3), 11.7(1), and 8.4(1) K for $Pr_3Pd_6Sb_5$, $Nd_3Pd_6Sb_5$, and $Gd_3Pd_6Sb_5$, respectively.

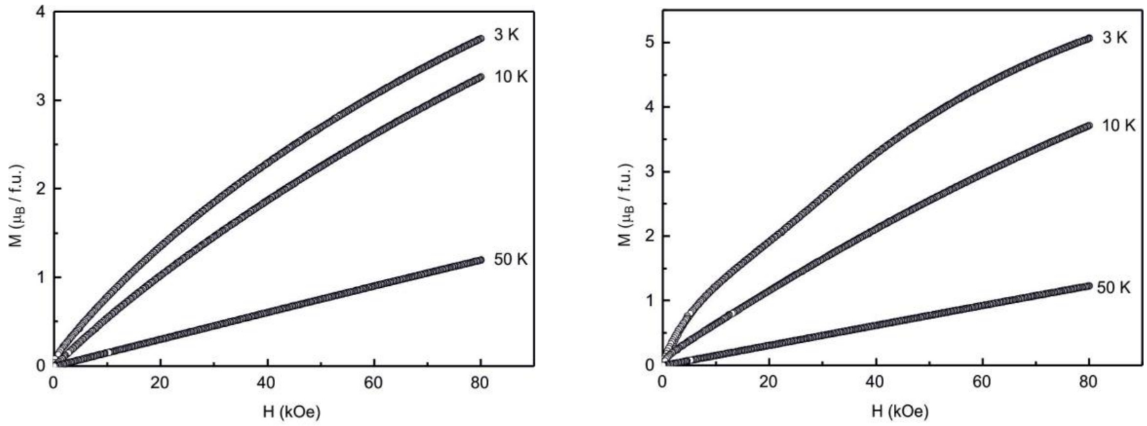

a) $Pr_3Pd_6Sb_5$

b) $Nd_3Pd_6Sb_5$

c) $Gd_3Pd_6Sb_5$

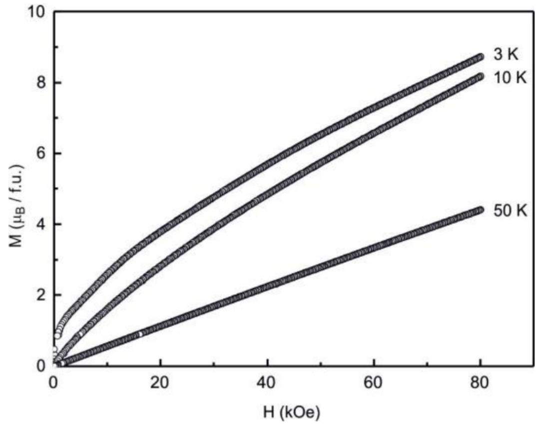

Fig. 9. Field-dependent magnetization isotherms M of a) $Pr_3Pd_6Sb_5$, b) $Nd_3Pd_6Sb_5$ und c) $Gd_3Pd_6Sb_5$ measured at 3, 10 and 50 K.

Fig. 9 displays the magnetization isotherms of a) $Pr_3Pd_6Sb_5$, b) $Nd_3Pd_6Sb_5$ und c) $Gd_3Pd_6Sb_5$ measured at 3, 10 and 50 K, with an applied external field between 0 and 80 kOe. The isotherms at 50 K show linear dependence of the magnetization on the applied field as is expected for paramagnetic materials. In case of a) $Pr_3Pd_6Sb_5$ and c) $Gd_3Pd_6Sb_5$ the isotherms at 3 and 10 K show only a slight curvature without any tendency of saturation. In case of b) $Nd_3Pd_6Sb_5$ the 3 K isotherm shows a minute sigmoidal course. This is indicative of spin reorientations. In addition, the 3 K isotherms of b) $Nd_3Pd_6Sb_5$ and c) $Gd_3Pd_6Sb_5$ exhibit a small hysteresis in the region 0 – 5 kOe and 0 – 1.5 kOe, respectively.

Acknowledgement

This work was financially supported by the Deutsche Forschungsgemeinschaft.

---

[1] Z. Ban, M. Sikirica, *Acta Crystallogr*. **1965**, *18*, 594.
[2] B. Eisenmann, N. May, W. Müller, H. Schäfer, *Z. Naturforsch*. **1972**, *27b*, 1155.
[3] K. R. Andress, E. Alberti, *Z. Metallkd*. **1935**, *27*, 126.
[4] E. Parthé, L. Gelato, B. Chabot, M. Penzo, K. Cenzual, R. Gladyshevskyy, TYPIX – *Standardized Data and Crystal Chemical Characterization of Inorganic Structure Types, Gmelin Handbook of Inorganic and Organometallic Chemistry*, 8th edition, Springer, Berlin, **1993**.
[5] P. Villars, K. Cenzual, *Pearson's Crystal Data: Crystal Structure Database for Inorganic Compounds* (release 2009/10) ASM International®, Materials Park, Ohio (USA) **2010**.
[6] D. Kußmann, R. Pöttgen, U. Ch. Rodewald, C. Rosenhahn, B. D. Mosel, G. Kotzyba, B. Künnen, *Z. Naturforsch*. **1999**, *54b*, 1155.
[7] R. A. Gordon, F. J. DiSalvo, R. Pöttgen, *J. Alloys Compd*. **1995**, *228*, 16.

[8] Yu. Grin, M. Ellner, B. Predel, K. Peters, *J. Alloys Compd.* **1993**, *201*, 209.

[9] R. Pöttgen, *Z. Naturforsch.* **1995**, *50b*, 175.

[10] I. Schellenberg, R.-D. Hoffmann, C. Schwickert, R. Pöttgen, *Solid State Sci.* **2011**, *13*, 1740.

[11] D. Johrendt, H. Hosono, R.-D. Hoffmann, R. Pöttgen, *Z. Kristallogr.* **2011**, *226*, 435.

[12] A. Imre, A. Mewis, *Z. Naturforsch.* **2006**, *61b*, 17.

[13] M. L. Fornasini, P. Manfrinetti, D. Mazzone, P. Riani, G. Zanicchi, *J. Solid State Chem.* **2004**, *177*, 1919.

[14] R. Pöttgen, Th. Gulden, A. Simon, *GIT Labor-Fachzeitschrift* **1999**, *43*, 133.

[15] D. Niepmann, Yu. M. Prots', R. Pöttgen, W. Jeitschko, *J. Solid State Chem.* **2000**, *154*, 329.

[16] K. Yvon, W. Jeitschko, E. Parthé, *J. Appl. Crystallogr.* **1977**, *10*, 73.

[17] W. K. Hofmann, W. Jeitschko, *Monatsh. Chem.* **1985**, *116*, 569.

[18] J. Emsley, *The Elements*, Oxford University Press, Oxford **1999**.

[19] H. Bärnighausen, *Commun. Math. Chem.* **1980**, *9*, 139.

[20] H. Bärnighausen, U. Müller, *Symmetriebeziehungen zwischen den Raumgruppen als Hilfsmittel zur straffen Darstellung von Strukturzusammenhängen in der Kristallchemie*, University of Karlsruhe and University/GH Kassel, **1996**.

[21] U. Müller, *Z. Anorg. Allg. Chem.* **2004**, *630*, 1519.

[22] U. Müller in *International Tables for Crystallography*, Volume A1, *Symmetry relations between space groups*, (Eds.: H. Wondratschek, U. Müller), 2^{nd} ed., chapter 1.6, **2010**, pp. 44 – 56.

[23] J. Donohue, *The Structures of the Elements,* Wiley, New York **1974**.

[24] R.-D. Hoffmann, R. Pöttgen, *Z. Kristallogr.* **2001**, *216*, 127.

[25] D. Kußmann, R.-D. Hoffmann, R. Pöttgen, *Z. Anorg. Allg. Chem.* **1998**, *624*, 1727.

[26] R. Pöttgen, R.-D. Hoffmann, R. Müllmann, B. D. Mosel, G. Kotzyba, *Chem. Eur. J.* **1997**, *3*, 1852.